

# Realistic MHD Modelling of Wind-Driven Processes in Cataclysmic Variable-Like Binaries

Alex Lascelles<sup>1,2</sup>

<sup>1</sup>*Physics & Astronomy Department, University of Southampton, Southampton, Hampshire, SO17 1BJ, UK*

<sup>2</sup>*Harvard-Smithsonian Center for Astrophysics, 60 Garden Street, Cambridge, MA 02138, USA*

13 May 2017

## ABSTRACT

The orbital evolution of cataclysmic variables with periods above the “period gap” ( $\geq 3.2$  hours) is governed by angular momentum loss via the magnetised wind of the unevolved secondary star. The usual prescription to study such systems takes into account only the magnetic field of the secondary and assumes its field is dipolar. It has been shown by Cohen et al. (2012) that introduction of the white dwarf and its magnetic field can significantly impact the wind’s structure, leading to a change in angular momentum loss rate and evolutionary timescale by an order of magnitude. Furthermore, the complexity of the magnetic field can drastically alter stellar spin-down rates. We explore the effects of orbital separation and magnetic field configuration on mass and angular momentum loss rates through 3-D magneto-hydrodynamic simulations. We find that inclusion of the white dwarf can reduce mass loss and angular momentum loss rates by up to factors of four and six respectively, when compared to a single secondary star case. Therefore, we find lower rates than the order of magnitude difference found previously, which we suggest is due to using a more physically realistic wind model that is verified by solar observations. A larger reduction in mass loss for stronger WD magnetic fields is observed and in general, anti-aligned dipolar configurations result in a further reduction. This is due to higher and anti-aligned dipolar magnetic fields more easily capturing ionised material and creating areas of closed field lines which reduce the amount of mass escaping the system. We argue that this reduction should be considered in future calculations for cataclysmic variable orbital evolution which include an AML prescription. White dwarf wind accretion rates decrease as orbital separation increases and for all cases, we find accretion rates of the order of  $10^{-14} M_{\odot} \text{yr}^{-1}$ . For the majority of cases, we find that accretion is most efficient for anti-aligned magnetic field configurations for the same reason that anti-aligned cases more easily close magnetic field lines in the areas in front of and behind the white dwarf.

## 1 INTRODUCTION

Cataclysmic variables (CVs) are close binary systems, normally consisting of a tidally locked, synchronously rotating secondary star which donates matter via an accretion disk onto a non-synchronously rotating white dwarf (WD). Their orbital and mass transfer evolution is believed to be largely controlled by the existence of two main angular momentum loss (AML) processes which dominate on either side of the so-called CV “period gap”. The period gap (see Figure 1) represents an empirical lack of systems with orbital periods between  $P_{orb} \approx 2.0$  hours and  $P_{orb} \approx 3.0$  hours. Below the gap, AML is driven purely by gravitational radiation, whilst above the gap it is primarily associated with the magnetised wind of the unevolved late-type donor star (Kraft et al. 1962; Verbunt & Zwaan 1981). The latter, referred to

as magnetic braking (MB), occurs when matter contained within the magnetised wind becomes decoupled from the secondary; this results in a braking torque which removes angular momentum from the system (Schatzman 1962; Mestel 1999). It is currently believed that the termination of MB after the secondary becoming fully convective causes mass transfer from the secondary to the WD to cease, resulting in the Roche lobe losing contact (Knigge 2011). CVs will then evolve as two separate orbiting bodies down through the period gap until the Roche lobe connects the system again and mass transfer begins, which occurs at the period gap’s lower edge. While the gravitational radiation dominated regime is well understood within the standard model for CV evolution, there is still no comprehensive theory for AML above the period gap (Rappaport et al. 1983; Andronov et al. 2003; Ivanova & Taam 2003). CVs are also believed to be a progen-

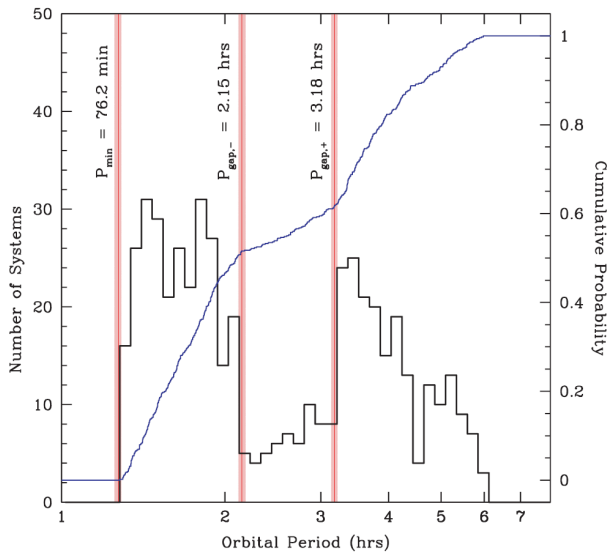


**Figure 1.** The number of CV systems is plotted against their orbital period. We observe the CV period gap at 2.15 – 3.18 hours. In nature, we find a lack of CVs with periods between these values. The blue curve shows how the cumulative probability of finding a CV with a certain period flattens out within the period gap. Below this gap, AML is controlled by gravitational processes whilst above this gap lies the regime in which we are considering, where MB is the main AML process. Figure taken with permission (Knigge 2006).

itor for Type Ia supernovae, and undergo novae explosions. Type Ia supernovae have long been used as standardisable candles for measuring extragalactic distances, and were used to prove that the expanding universe is accelerating (Riess et al. 1998). Therefore, understanding CV evolution is of considerable importance.

This AML process above the period gap occurs at the Alfvén surface, the collection of points where wind material has sufficient velocity to decouple from the host. The Alfvén surface is defined by a Mach number of 1, where the Mach number is given by,

$$M = \frac{\sqrt{U_x^2 + U_y^2 + U_z^2}}{V_a}, \quad (1)$$

where  $U_x$ ,  $U_y$ , and  $U_z$  are the three components of wind velocity, and  $V_a$  is the Alfvén velocity. In turn, the Alfvén velocity is given by,

$$V_a = \sqrt{\frac{B_x^2 + B_y^2 + B_z^2}{4\pi\rho}}, \quad (2)$$

where  $B_x$ ,  $B_y$ , and  $B_z$  are the three components of the magnetic field strength, and  $\rho$  is the mass density. Within the Alfvén surface, the wind is considered sub-Alfvénic and it transitions to super-Alfvénic outside of this surface.

MB is dependent on the large-scale stellar magnetic field. This determines the mass loss (ML) rate due to the stellar wind, and as a consequence, the AML rate (e.g., Weber & Davis 1967; Mestel 1968; Kawaler 1988). Measuring stellar winds, ML, and AML observationally for close binary systems poses significant difficulties. We cannot directly observe the stellar winds for such systems and so rely on observational measurements to infer the wind accretion and

subsequently the ML rate, such as metal lines caused by the stellar wind interacting with the interstellar medium. Moreover, for rapidly rotating systems for which proxies such as X-ray emission can be used to infer magnetic properties, even larger uncertainties arise due to X-ray saturation and supersaturation affecting spin-down rates (e.g., Andronov et al. 2003; Ivanova & Taam 2003; Barnes 2003; Wright et al. 2012). A modelling approach is a better way to investigate these properties, as we can explore many different parameters and physical mechanisms, and associate the solutions with a particular set of these initial conditions. Magnetohydrodynamic (MHD) models are especially useful as they allow us to directly simulate the interaction between the coronal magnetic field and the coronal and wind plasma. The interplay of these features is what determines the extent of the MB — the phenomena that we are most interested to understand.

The current assumption is that MB for CV systems follows the same process as for single stars, thus the inclusion of the WD should make no difference to AML regimes (e.g., Rappaport et al. 1983; Andronov et al. 2003; Ivanova & Taam 2003; Davis et al. 2008; Knigge 2011). However, it has been shown by Cohen et al. (2012) that the presence of the WD physically blocks and restructures the stellar wind, altering the Alfvén surface shape and size, resulting in changes in ML and AML rates of up to an order of magnitude.

The stellar wind also accretes onto the WD at a rate that can be modulated by the binary separation and stellar magnetic fields. This is important because wind accretion in pre-cataclysmic binaries has been used to infer the wind-driven mass loss rate in late-type dwarfs (e.g., Debes 2006; Drake et al. 2014), which is notoriously difficult to measure by other means because the winds themselves are too weak to be detected directly. For example, Wood et al. (2001) are only able to place an upper limit on the mass loss of Proxima Centauri by using Hubble Space Telescope Ly  $\alpha$  spectra and probing the interaction of the stellar wind with the interstellar medium. Without any simulation available, the prescription for finding the stellar mass loss rate is to assume the WD accretes according to the Bondi-Hoyle formula (Bondi & Hoyle 1944),

$$\dot{M}_{\text{Acc}} = \frac{4\pi G^2 M_{\text{WD}}^2 \rho(r)}{v^3}, \quad (3)$$

where  $G$  is the gravitational constant,  $M_{\text{WD}}$  is the WD mass,  $\rho(r)$  is the wind mass density at radius  $r$ , and  $v$  is the stellar wind velocity. Following Matranga et al. (2012), we can make the replacement,

$$\rho = \frac{\dot{M}}{4\pi v R_\star^2}, \quad (4)$$

where  $\dot{M}$  is the total mass loss rate for the system,  $R_\star$  is the secondary star radius, and  $v$  is approximately the escape velocity for the secondary,  $v_{\text{esc}} \approx \sqrt{2GM_\star/R_\star}$ . Therefore, we arrive at a WD accretion rate given by,

$$\dot{M}_{\text{Acc}} = \left( \frac{R_\star M_{\text{WD}}}{2aM_\star} \right)^2 \dot{M}, \quad (5)$$

where  $a$  is the binary separation and  $M_\star$  is the mass of the secondary. This equation serves as a good order of magnitude estimate, and we plot it alongside our results to see how the accretion rates calculated from the MHD simulations

provide us with a better tool for calculating wind accretion rates.

Solid bodies placed within a flow can be subject to vortices and flow instabilities. One example in 2-D flows is the Kármán vortex street effect, a pattern of vortices caused by the unsteady separation of flow from the body. This effect is what causes suspended power lines to “sing” as the wind passes over them and what causes a beach ball to wobble through the air when hit with a considerable force. The flow behind the body is made to oscillate from side to side after it passes over the surface of the body. The same effect may be present for a WD situated in a stellar wind and in Section 4, we discuss the possibility of this effect appearing in our simulation solutions.

In this study, we build upon the work outlined in Cohen et al. (2012), to produce a more extensive grid of test cases. We include a secondary star at the origin, and choose to vary the distance of the WD. We investigate the WD wind accretion over all separations and field permutations that we simulate. The mass of the WD causes some matter to be gravitationally attracted and the WD’s magnetic field captures charged material from otherwise open field lines. The combination of these processes results in wind accretion onto the WD. We use a more physically realistic MHD model than the models used in the work by Cohen et al. (2012). Those models used a prescription for wind acceleration based on the Wang–Sheeley–Arge observation of wind acceleration on the Sun being correlated with a field expansion factor (Arge & Pizzo 2000; Wang & Sheeley 1990). The interaction of the WD and secondary field will change the wind acceleration in ways that are most likely non-physical. Here, we use the more physically accurate BATS-R-US model to investigate new orbital separations and WD magnetic field strengths and orientations, and for the first time, include a detailed study of the accretion.

In Section 2 we present our numerical approach and the grid of parameters investigated. In Section 3 we present our results and their implications are discussed in Section 4. Our findings are concluded and I present avenues for possible further work in Section 5.

## 2 SIMULATION

### 2.1 Model

All numerical solutions obtained and discussed herein are acquired using the generic BATS-R-US MHD model (Powell et al. 1999), which is part of the Space Weather Modeling Framework (SWMF; Tóth et al. 2012). The SWMF is a collection of physical models that primarily work in the regime of solar and space physics but can be extended for use in other areas. Here, we use the solar corona component (van der Holst et al. 2014) to simulate the stellar corona and stellar wind for the WD and secondary star binary system. The model is driven by surface magnetic field maps (magnetograms) which allow the calculation of the potential magnetic field distribution above the secondary star surface; this solution serves as the initial condition for the magnetic field. Once the potential field is found, a set of MHD conservation equations for mass, momentum, magnetic induction, and energy are solved. The model self-consistently calculates the coronal heating and the wind acceleration under

the assumption that it is due to Alfvén wave turbulence dissipation. We use Alfvén wave turbulence dissipation as it is currently the favoured mechanism for driving the solar wind, and the BATS-R-US model has been calibrated against this, using observations of the solar wind. Radiative cooling and electron heat conduction are also taken into consideration. For this study, the magnetograms used were purely theoretical and took the form of perfect dipoles.

The MHD code outputs a self-consistent solution for the magnetised wind of the secondary star and the WD is incorporated as an additional boundary condition on the magnetic field, density, and temperature. Ordinarily, the MHD code would encounter significant numerical difficulties around the WD due to the combination of its small size and very large surface magnetic fields. In order to avoid this, we increase the WD size (with appropriate scaling down of the surface field) from Earth-like ( $\sim 0.01R_{\odot}$ ) to  $0.2R_{\odot}$ . This is justified as the effect of the WD on the system is not dependent on the structure of the body but rather on properties such as its mass, dipole moment, and position (Cohen et al. 2012).

We perform many cases of time-independent simulations and a time-dependent simulation. For *time-independent* simulations, the system is assumed to be in a steady state which does not depend on time. The simulation advances by performing a certain number of iterations. The time-step on which the simulation iterates is allowed to be different for all of the cells in the domain. The time step is determined by the code based on cell parameters. *Time-dependent* simulations allow the parameters involved to progress with time and the smallest time-step is applied to all of the cells, giving a more accurate solution at the expense of being more computationally demanding and requiring a longer time to run. For this reason, we chose to perform mostly time-independent simulations first, followed by time-dependent simulations once the parameter space was better understood. There is also a possibility for instabilities to occur when investigating a system like this using only time-independent simulations. In Section 3, I discuss how we decide to investigate time-dependent simulations after suspecting that some of the solutions may be unstable.

CVs are close binary systems. They normally consist of a tidally locked, synchronously rotating secondary, which donates matter via Roche lobe overflow and an accretion disk onto a non-synchronously rotating WD. In this study, we treat a simplified synchronous, disk-less case that is also appropriate for pre-cataclysmic, detached close binaries comprised of a late-type dwarf and WD. Investigation of the complete, non-synchronous case is much more computationally demanding, requiring a time-dependent MHD simulation outside of the scope of this work. We ignore any centrifugal effects and assume the bodies to be spherical, with no tidal stretching. All time-independent solutions are steady state and the orbital configuration for all cases is visualised in the rotating frame. We choose not to include any Adaptive Mesh Refinement (AMR) to continually change the grid size in areas of higher turbulence as the simulation progresses. Instead, we adopt a spherical grid of radius  $60.0R_{\odot}$ , with additional mesh refinements in a box extending around the WD so that higher resolution ( $\Delta x \approx 0.01R_{\odot}$ ) is achieved in this more important region. This acts to reduce the total computation time and allows us to simulate many more

cases than if a grid with a high mesh refinement throughout was used.

To efficiently utilise this computationally demanding model, I use the Smithsonian Institution High Performance Cluster, named “Hydra” — a Beowulf cluster with more than 3,000 CPU cores and RAM exceeding 18TB. With Hydra, I perform a single simulation in parallel across 500 cores and then repeat this process for each simulation in my set. I begin by defining values in a parameter file such as how long I want the simulation to run, the binary separation distance, and WD magnetic field strength. I set the simulation running and it continues to run, saving output files at the cadence of my choosing, until it reaches the maximum simulation time allotted to my portion of the cluster, or it terminates at the chosen iteration. Upon completion, the code generates restart files, which are a copy of all the run parameters at that point in the simulation. These are used if it is necessary to restart a run from a previous solution. 2-D and 3-D solutions are saved throughout the simulation and all the information on how the runs progress is contained within a run log file. After each run, I save these solutions, the run log, and the restart files before beginning a new simulation. Using 500 cores, a single simulation can take up to 15 – 26 hours to run, depending on which nodes it decides to begin on.

## 2.2 Methodology

In the simulation box, I place the secondary at the origin and the WD at varying displacements along the  $x$ -axis. Intrinsic parameters for the secondary’s radius, mass, and equatorial field strength are  $R_\star = 1.0R_\odot$ ,  $M_\star = 1.0M_\odot$ , and  $B_\star = 10G$  respectively. The corresponding parameters for the WD are  $R_{WD} = 0.2R_\odot$ ,  $M_{WD} = 0.5M_\odot$ , and  $B_{WD} = 10G$ . However,  $B_{WD}$  and  $M_{WD}$  are parameters we change in our test cases. We use a slightly larger secondary star radius than is found in normal CVs, which allows us to probe stronger effective fields whilst avoiding numerical difficulties. For example, the field for a  $1.0R_\odot$  star is the same as eight times the field for a  $0.5R_\odot$  star. The field strength is chosen due to the aforementioned necessary scaling up of the WD size so that  $B_{WD}$  is equivalent to an equatorial field strength of  $B \approx 10^5G$  at the true size of the WD. This value is slightly less than that of a magnetic CV but is chosen to allow the simulations to run without problem, and is high enough so that it substantially influences the single secondary star field. Weak fields do not make much of a difference to the single star solution, and strong fields are hard to simulate. Cohen et al. (2012) has shown that fields of the order of  $10^5G$  are high enough to produce a difference when compared to the single star case.

I select appropriate values for parameters such as the source surface, Poynting flux, and correlation length, so that the solutions will correctly converge. The source surface describes the distance at which magnetic fields will become radial, and is chosen to be at  $2.5R_\odot$ , which is close to the secondary so that it occurs before any interaction with the WD. The Poynting flux of outgoing Alfvén waves sets the boundary conditions for the Alfvén wave energy density, and is given by  $S_A = \omega V_A$ , where  $V_A$  is the Alfvén velocity and  $\omega$  is the Alfvén wave energy density. Simply speaking, the

	Mass ( $M_\odot$ )		Radius ( $R_\odot$ )		Field Strength ( $G$ )	
	SS	WD	SS	WD	SS	WD
Set A	1.0	0.5	1.0	0.2	10	10
Set B	1.0	1.0	1.0	0.2	10	10
Set C	1.0	0.5	1.0	0.2	10	50

**Table 1.** Summary of the sets of test cases carried out in this study. I show the mass, radius, and field strength for the secondary star (SS) and white dwarf (WD). Set A represents the initial case examined, with parameters  $R_\star = 1.0R_\odot$ ,  $M_\star = 1.0M_\odot$ , and  $B_\star = 10G$  for the secondary and  $R_{WD} = 0.2R_\odot$ ,  $M_{WD} = 0.5M_\odot$ , and  $B_{WD} = 10G$  for the WD. In Set B, we change the mass of the WD to be  $1.0M_\odot$  and in Set C, we take Set A and increase the field strength to 50 Gauss. Sets B and C are done in order to investigate how WD mass and magnetic field strength influences overall ML and AML rates.

correlation length,  $L_\perp$ , is equal to the size of the largest eddies allowed in the turbulent flow of the stellar material.

We perform several test cases to investigate the effects of orbital separation as well as WD magnetic field strength and alignment. These are illustrated above in Table 1. For each set, we explore many different separations in the range  $3.0 - 8.0R_\odot$ . Details of the separations chosen are given in Section 3. One additional case with just a single secondary star and no WD is made to serve as reference model.

For each simulation, I obtain a steady state solution in a 2-D ( $y = 0$ ) and a 3-D form, which I view using the Tecplot 360 EX software. The  $y = 0$  cut refers to a plane of the full 3-D solution containing only points on the  $x$  and  $z$  axes. This plane is primarily used to observe how the magnetic field distribution and global wind features differ between cases. The 3-D view, however, is used to view the full 3-D Alfvén surfaces and the accretion onto the WD. Tecplot allows for programming of equations describing physical parameters of interest such that these can be extracted and visualised. In this way, parameters of interest such as wind velocity, Alfvén velocity, and mass flow can be calculated at each point throughout the entire 3-D domain. Performing integrations over certain areas of the domain for the 3-D solutions allows the WD accretion rate and global ML and AML rates to be calculated. Our results fall within the main categories of mass and angular momentum loss and WD accretion, and are presented in the following section.

To calculate the ML rate, I take the 3-D solution, and create spherical zones near the boundary of the domain at  $58.0R_\odot$ . I then perform a scalar flow rate integration over these spheres for the  $\dot{M}$  parameter in order to calculate how much net mass in  $gs^{-1}$  is entering or leaving the system. The ML rate,  $\dot{M}$ , is given by

$$\dot{M} = \int \rho U_r dS, \quad (6)$$

where  $\rho$  is the mass density,  $S$  is the surface to be integrated over, and  $U_r$  is the stellar wind velocity in the radial direction. As a quality check, I calculate the same value at smaller spheres of  $50.0R_\odot$  and  $40.0R_\odot$  to ensure that the value is consistent, as the total mass and hence total ML must be conserved. The process is similar for the AML, except the surface which must be integrated over is the Alfvén surface and the parameter over which this is carried out is  $\dot{J}$ . The AML rate,  $\dot{J}$ , is defined as,

$$\dot{J} = \int \Omega_\star \rho R^2 \sin(\theta) dA, \quad (7)$$

where  $\Omega_*$  is the stellar rotation rate,  $R$  is the radial distance from the secondary,  $\theta$  is the angle from the rotation axis, and  $A$  is the Alfvén surface. I use Equations 6 and 7 to calculate a scalar flow integral over the domain boundary and the Alfvén surface respectively.

The WD accretion rate is calculated similarly, except a scalar integral is calculated over a set of spheres around the WD for the mass flow parameter,  $M_{\text{Flow}}$ , given by,

$$M_{\text{Flow}} = \frac{(X - X_{\text{WD}})U_x + YU_y + ZU_z}{\sqrt{(X - X_{\text{WD}})^2 + Y^2 + Z^2}} \rho, \quad (8)$$

where  $X$ ,  $Y$ , and  $Z$  are the distances along the three axes,  $X_{\text{WD}}$  is the distance along the x-axis for the WD, and  $U_x$ ,  $U_y$ , and  $U_z$  are the wind velocities in the x, y, and z directions respectively. The expression  $(X - X_{\text{WD}})$  is included as we wish to calculate the mass flow using the WD as the origin and not the secondary star. I construct five shells around the WD, of radii ranging from  $0.5 - 1.5R_{\odot}$ , and calculate the integrated mass flow through the entire surface for each to find the WD accretion rate.

### 3 RESULTS

In this section, we present our full set of time-dependent and time-independent simulations. All  $y = 0$  simulation figures are either coloured by wind velocity (in  $\text{km s}^{-1}$ ) or density (in  $\text{g cm}^{-3}$ ), with the magnetic field lines represented as arrowed black lines and the Alfvén surface as a solid white line. The larger white circle at the origin is the secondary whilst the smaller white circle is the WD. The iteration at which the simulation was stopped at is indicated in the upper right corner of the figures, as is the value of the binary separation in solar radii and WD magnetic field in Gauss.

#### 3.1 Single Secondary Star Case

In order to understand the results of the CV-like system with varying WD separations and magnetic field strengths, we first need a comparison case which does not include the WD. We perform a simulation consisting of simply a single secondary star with the parameters:  $R_* = 1.0R_{\odot}$ ,  $M_* = 1.0M_{\odot}$ , and  $B_* = 10\text{G}$ . This is illustrated in Figure 2 after 40,000 iterations of the MHD code with the secondary star located at the origin. We use this solution to discover if the addition of the WD really does have an impact on the wind structure and on mass and angular momentum loss rates.

#### 3.2 Set A Simulations

With the single secondary stellar wind comparison established, we begin the simulations in Set A — as shown in Table 1. We choose a range of separations from  $3.0 - 8.0R_{\odot}$  in mostly  $1.0R_{\odot}$  increments except for the cases at  $4.5R_{\odot}$ ,  $5.5R_{\odot}$ ,  $5.8R_{\odot}$ ,  $6.2R_{\odot}$ , and  $6.5R_{\odot}$ . These were chosen because they were situated around what was previously initially thought to be an interesting case — an area of abnormally low ML. However, this is later shown to be in accordance with the overall ML trend (see Section 4.2). The minimum separation chosen was  $3.0R_{\odot}$  because of the simulation beginning to crash due to numerical issues such as insufficient spatial or time resolution when the WD approaches

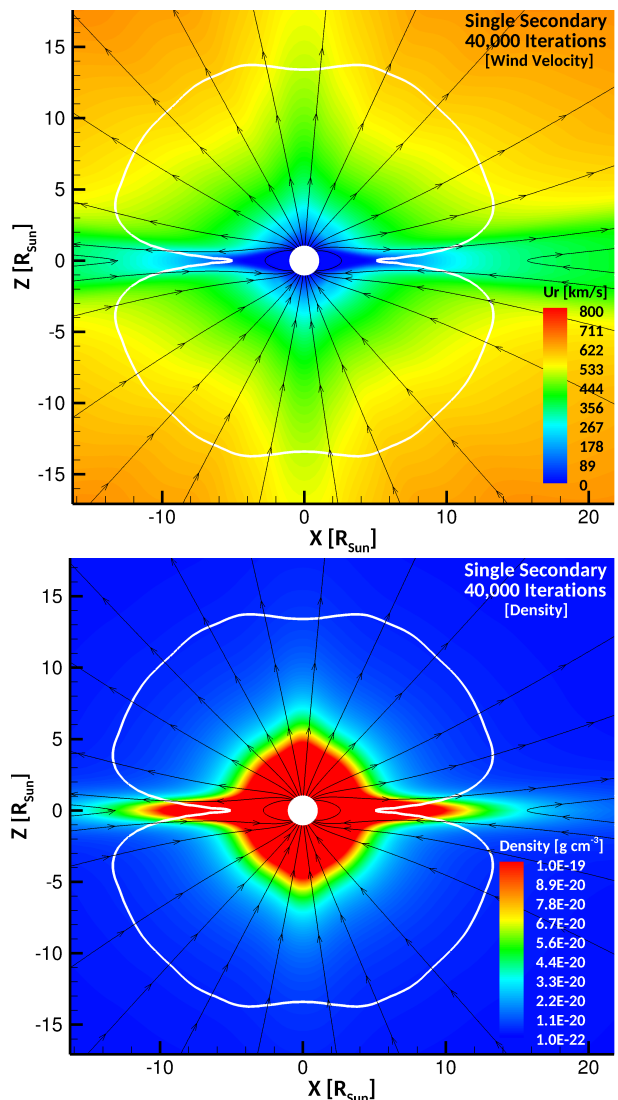


**Figure 2.** The  $y = 0$  meridional cut through the 3-D solutions for a single secondary star, with a structure reflecting that of a perfect dipole. The upper panel shows the solution, coloured by wind velocity (in  $\text{km s}^{-1}$ ), with the magnetic field lines represented as arrowed black lines and the Alfvén surface as a solid white line. The lower panel shows the same but coloured by mass density (in  $\text{g cm}^{-3}$ ).

the secondary star surface too closely. In theory, the maximum separation could be extended indefinitely. However, at some large binary separation, the solution converges to that of the single secondary star case when the WD magnetic field becomes far enough from the secondary such that it cannot substantially divert any charged material from the stellar wind.

For each separation, we perform a simulation for the cases of a WD magnetic field both aligned and anti-aligned with the secondary field, notated as  $B = -10\text{G}$  (aligned) and  $B = 10\text{G}$  (anti-aligned). We investigate both alignments to observe the effect on ML and the wind environment of a flipped magnetic field alignment. This occurs naturally in some circumstances, such as the 11-year solar cycle. Cyclic magnetic activity is also an observed feature of stellar dy-

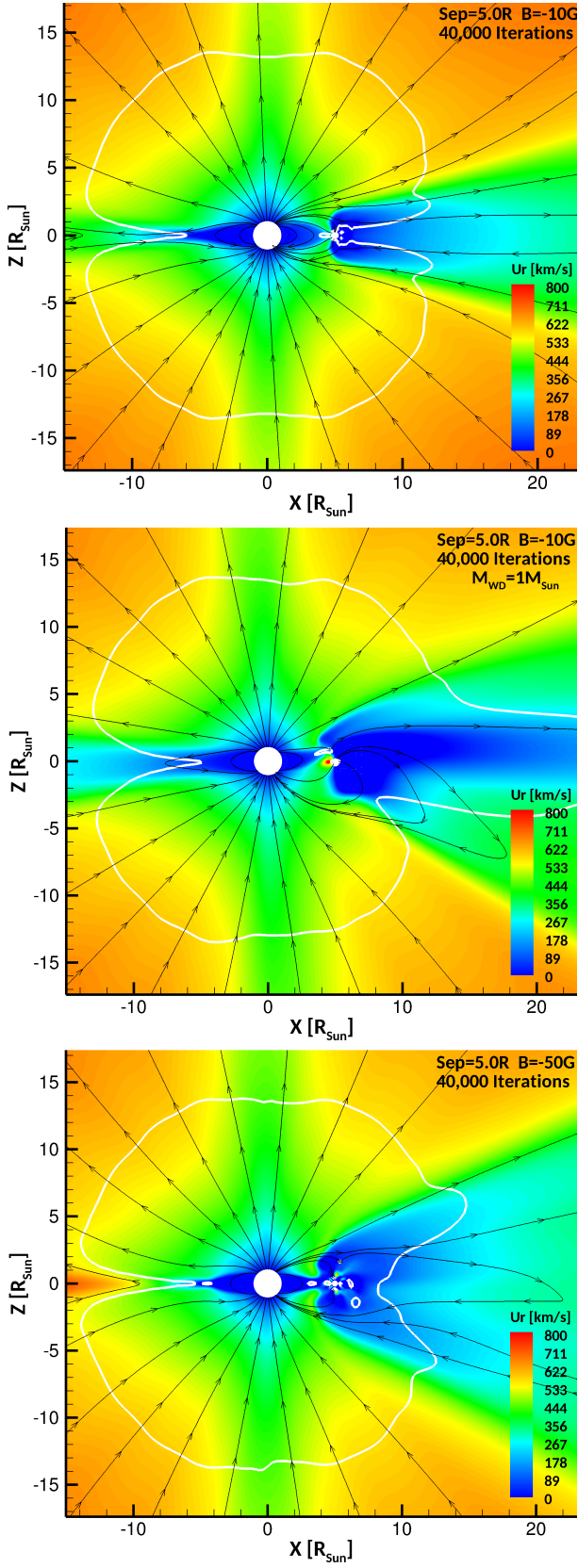


**Figure 3.** Three cases are shown with *aligned* WD magnetic fields and are coloured by **wind velocity**, with the magnetic field lines represented as black lines and the Alfvén surface as a white line. From the top panel down, they represent the orbital separation of  $5.0R_{\odot}$  for the Set A, B, and C cases respectively. The middle panel shows some asymmetry in the solution which could suggest that the problem is unstable (see Section 3.5).

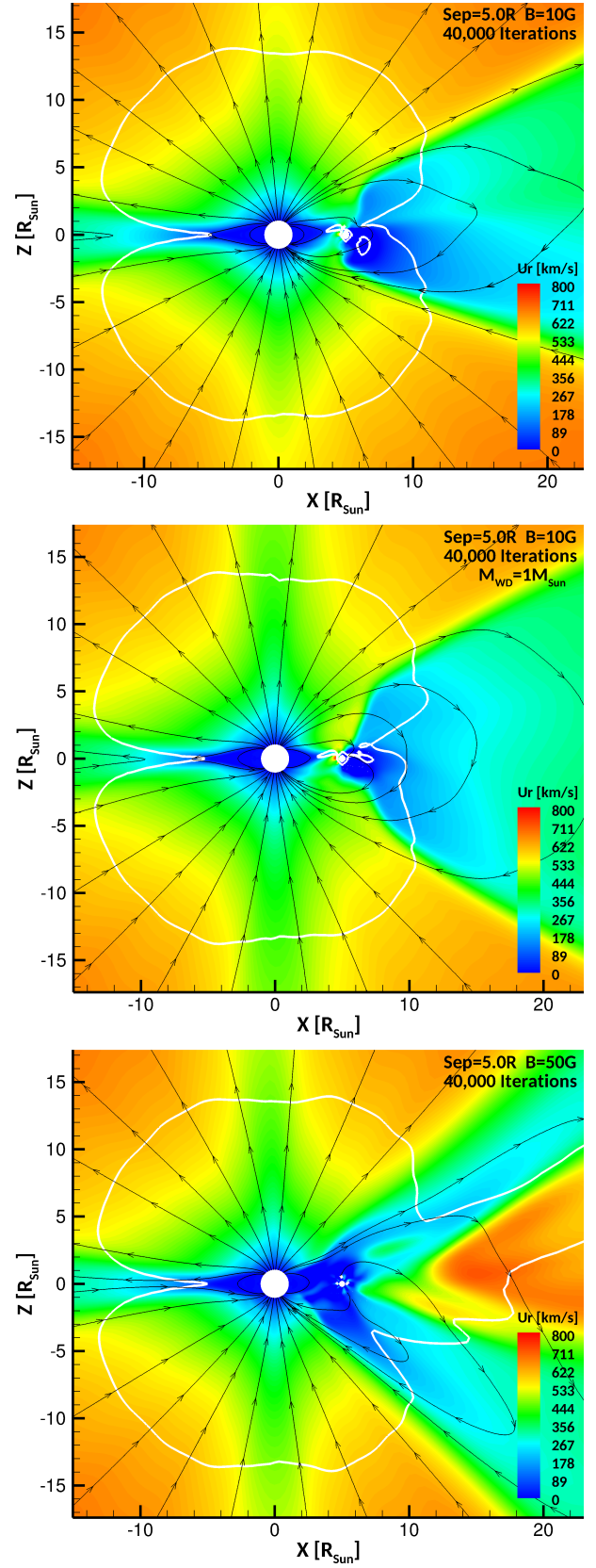


**Figure 4.** The same three cases are shown but with *anti-aligned* WD magnetic fields. From the top panel down, they represent the orbital separation of  $5.0R_{\odot}$  for the Set A, B, and C cases respectively.

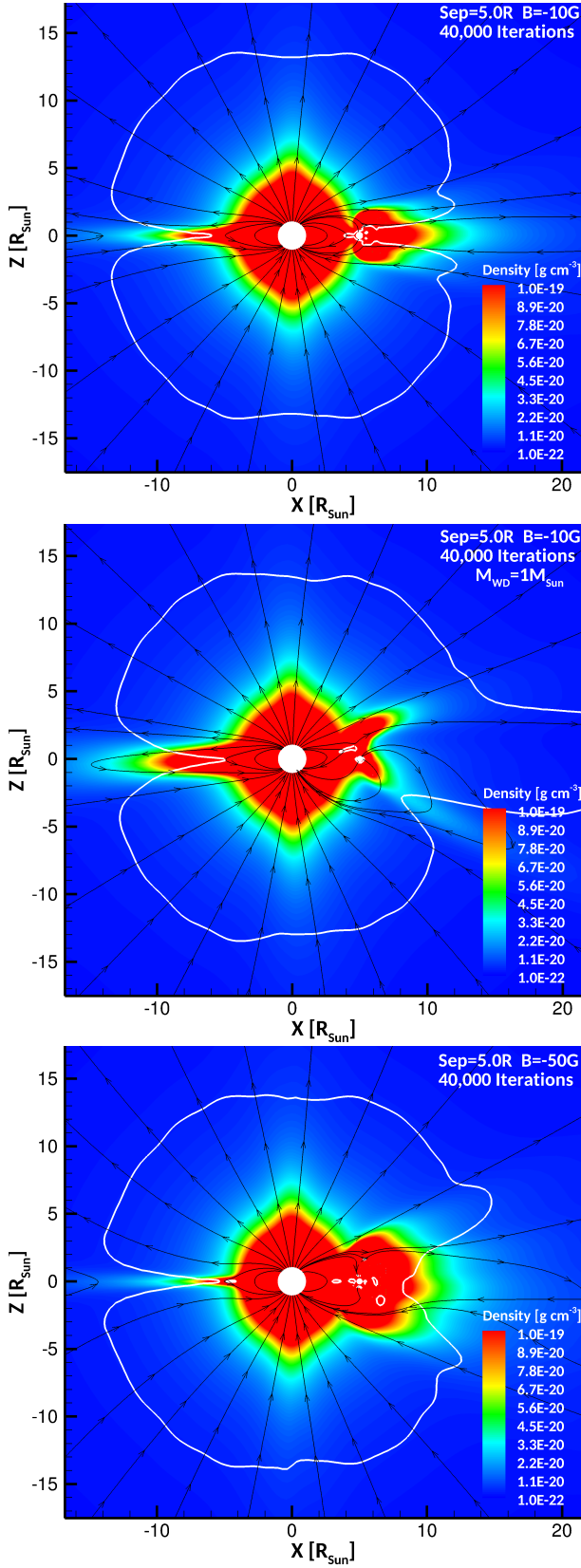


Figure 5. The same three cases are shown but with *aligned* WD magnetic fields and are coloured by **mass density**. From the top panel down, they represent the orbital separation of  $5.0R_{\odot}$  for the Set A, B, and C cases respectively.

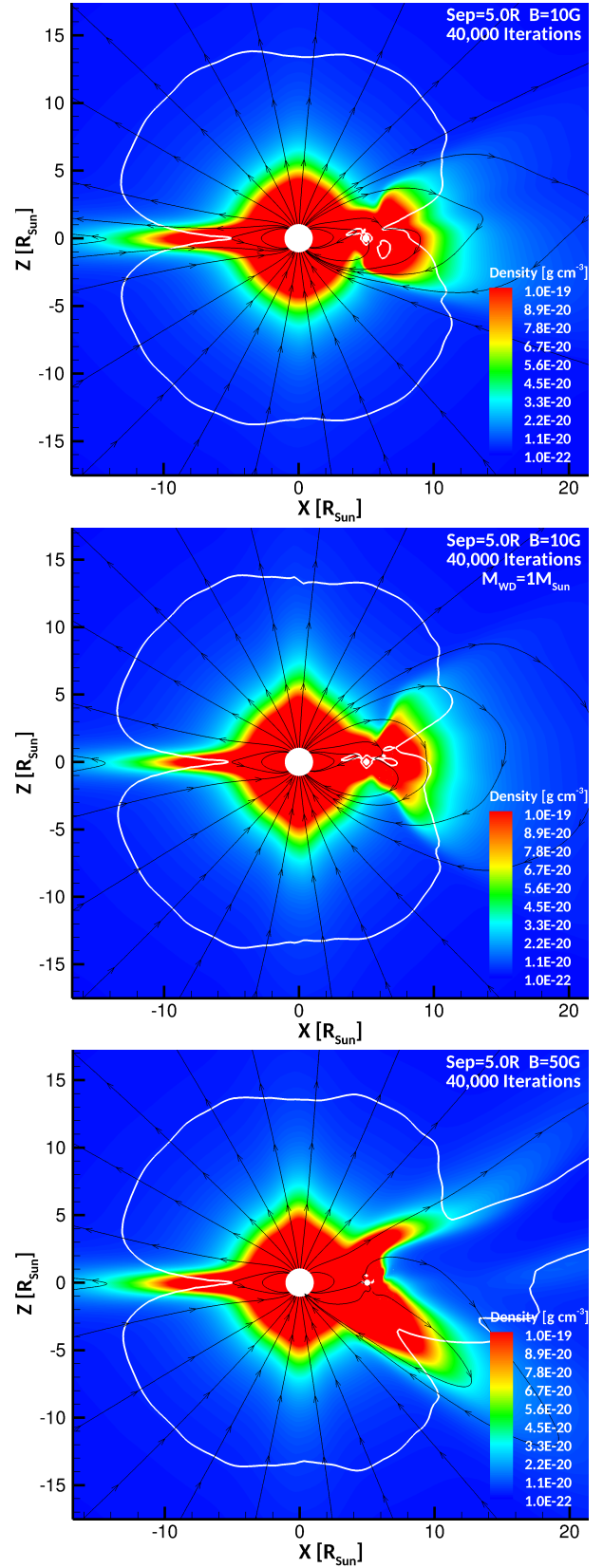
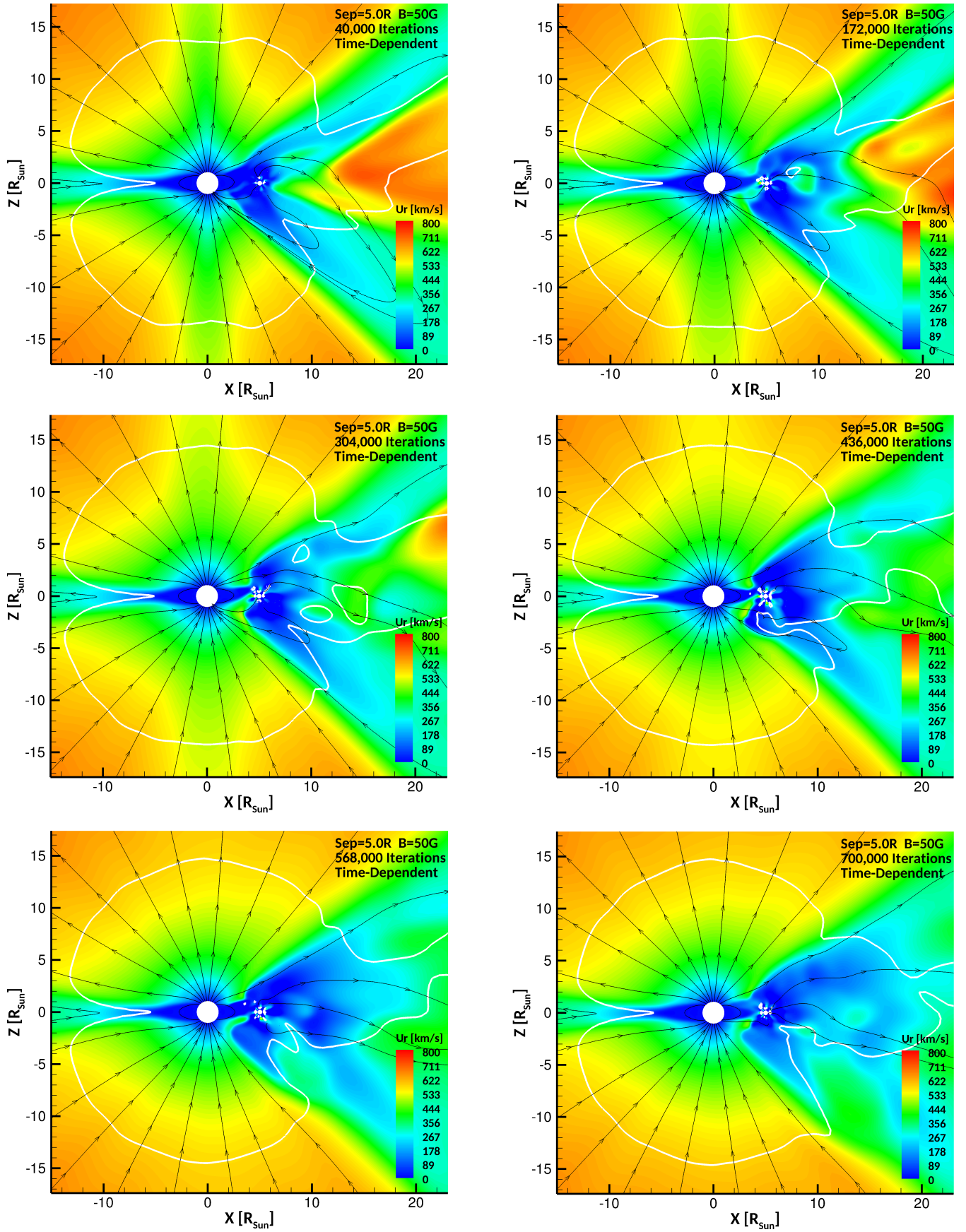


Figure 6. The same three cases are shown but with *anti-aligned* WD magnetic fields. From the top panel down, they represent the orbital separation of  $5.0R_{\odot}$  for the Set A, B, and C cases respectively.



**Figure 7.** Time-dependent simulations for the anti-aligned  $5.0R_{\odot}$  Set C case displayed as a snapshot every 2.5 hours of simulation time.

namos. The secondary star is expected to undergo cyclic activity analogous to that of the Sun, with an attendant field reversal; refer to (e.g., Wargelin et al. 2017) for detection of the cycle in the Proxima Centauri system. During a magnetic field reversal, the current sheet, a surface surrounding the star where the rotating stellar magnetic field induces an electrical current, becomes more distorted. This may lead to the increased intensity of space weather in the form of energetic particles, which are ordinarily partially blocked by the current sheet, but are now allowed to travel freely through the stellar system (Than 2013). Therefore, if applied to future studies, understanding how the wind environment changes due to a flipped magnetic field may also help us to predict the space weather environment for simulations of CVs including planetary bodies.

Figure 3 illustrates the effects of increasing binary separation on the stellar wind solution for the case of aligned magnetic dipoles and WD separation of  $5.0R_{\odot}$ . Three panels are shown, corresponding to the Set A, B, and C cases after 40,000 iterations. The same separations are shown for the case of *anti-aligned* WD magnetic dipolar field in Figure 4. This is done in order to understand the effect of the magnetic field alignment on the wind structure and ML. In both figures, the Set A cases are shown in the *top* panel. Figures 5 and 6 replicate Figures 3 and Figure 4 but show how mass density evolves instead of wind velocity. The implications of these solutions are discussed in Section 4.

### 3.3 Set B Simulations

To identify if changing the mass ratios of the WD and secondary produces a significant change in the wind structure, we investigate the case of the WD possessing a doubled mass of  $1.0M_{\odot}$ . We maintain the WD magnetic field strength at 10G and all of the other variables remain fixed so that we just explore the difference of mass ratio. In total, we perform five separations,  $3.0 - 7.0R_{\odot}$  for each magnetic field alignment. The middle panel of Figures 3 and 4 shows the wind velocity for aligned and anti-aligned Set B cases at an orbital radius of  $5.0R_{\odot}$ . The same solutions are shown for mass density in the *middle* panel of Figures 5 and 6.

### 3.4 Set C Simulations

To test how a different WD magnetic field strength changes the solution, we increased the magnetic field to 50G and ran simulations for separations of  $3.0 - 8.0R_{\odot}$  in integer steps. It became harder to test for small separations, as the combination of the secondary field and the larger WD field would cause the simulation to crash prematurely. The bottom panel of Figures 3 and 4 display the wind velocity for Set C cases at  $5.0R_{\odot}$  for the aligned and anti-aligned cases respectively. I illustrate the same solutions but for mass density in the *bottom* panel of Figures 5 and 6.

### 3.5 Time-Dependent Simulation

As the project developed, close examination of the results suggested that the situation might be unstable, and that a static solution might not capture all the details. We find that this is a dynamic problem, which in reality deserves a

time-dependent treatment. For this reason, we choose to run some time-dependent simulations. Some solutions are more stable than others, however, this is a hydrodynamic issue as explained in Section 1 by the Kármán vortex street effect; the simulations will naturally evolve like this. These time-dependent simulations show the true evolution of the system and the physical mechanisms involved, which we argue can be applied to the remaining data set. It may not be possible to reach a steady state solution due to the hydrodynamical instabilities caused by the simulation of an obstacle (the WD field) in a flow (the stellar wind).

To the best of our knowledge, this is the first time that fully 3-D time-dependent MHD simulations have been investigated for stellar winds around a WD in a CV-like system. Due to these simulations being very computationally heavy, we are only able to present one solution at this time. We simulate the case of opposite field alignment for Set C at  $5.0R_{\odot}$ . We choose this separation as it marks the middle value examined for all of the other datasets. Time-dependent simulations must be started from a restart file of a completed time-independent solution. We simulate for a total of 700,000 iterations, corresponding to a simulation time of 13.2 hours, and a physical time of over seven days. We intend to sample any instabilities as best we can, and a natural timescale is the wind crossing time. For a representative slower wind of approximately  $150 \text{ kms}^{-1}$  and a length scale of approximately  $10.0R_{\odot}$ , the crossing time is 12.9 hours. Therefore, this simulation time is sufficient to catch any changes in the solution. We choose to sample the simulation by saving  $y = 0$  files with a time step of 1 minute. As the radius of the WD is  $0.2R_{\odot}$  and the maximum wind speed we observe in this region is  $1000 \text{ kms}^{-1}$ , the time interval would be 2.3 minutes, making our time step sufficient.

Figure 7 shows a snapshot of the 50G case after every 132,000 iterations (2.5 hours). Time-dependent are the only types of simulation which accurately reflect the dynamic nature of the problem in hand and therefore are the most useful once a general trend is found through the running of time-independent simulations.

### 3.6 Analysis of the Solutions

With all the simulations complete, I now conduct a set of analyses to find the ML, AML, and WD wind accretion rates for each case. I plot the ML rate against separation for all solutions in Figures 8, 9, and 10. In Figures 11, 12, and 13, I plot the AML rate against separation.

As the secondary accelerates its stellar wind, some of the charged particles are sufficiently diverted by the WD magnetic field to be accreted onto the WD surface. This is known as wind accretion, as discussed in Section 1. After calculating the accretion rate for shells of different radii around the WD, I find that in general each shell in this range shows the same trend for wind accretion. Therefore, I choose the  $1.0R_{\odot}$  shell as it is the median radii, and in Figure 14, calculate the total wind accretion rate onto the WD in  $M_{\odot}\text{yr}^{-1}$  and plot this against WD orbital separation for Sets A, B, and C. Using the 3-D solutions, I am able to produce a colour plot of this accretion on a shell situated just above the WD surface to show the mass inflow and outflow (see Figures 15 and 16).

All of the figures discussed above show the difference

in ML, AML, and WD wind accretion rates as a result of a different magnetic field alignment, magnetic field strength, and binary separation and are discussed in Section 4.2.

## 4 DISCUSSION

In this section, we present our interpretations of the data and suggest the physical reasoning behind the trends and solutions we observe. Our results can be divided into two categories — mass and angular momentum loss, and WD wind accretion. These two categories are discussed in Sections 4.2 and 4.3 respectively. However, the simulation solutions are powerful results on their own, as they show how the wind structure evolves. They are discussed below. By analysing the structure and form of the  $y = 0$  solutions, we can learn something of the underlying physics and magnetohydrodynamics in a CV-like system. The  $y = 0$  plane is preferable as it samples the poles of the WD and secondary. We could examine any plane, but we restrict our analysis to this one as most of the salient properties of the solutions are present there.

### 4.1 2-D Solutions

#### 4.1.1 Single Secondary Star Case

In Figure 2, I present the wind solution for a single secondary star placed at the origin of our domain. We observe complete symmetry about the  $z = 0$  plane, and an Alfvén surface that is nearly spherical except for a pinch at the  $z = 0$  plane. This happens because the Alfvén velocity is proportional to the magnetic field, which is zero at the current sheet, so near the equatorial plane it is very small. If the Alfvén velocity is small, then the wind reaches it closer to the star and more quickly, so that is where the Alfvén surface will reside. Wind velocities range from  $0 - 200 \text{ km s}^{-1}$  very close to the secondary, with slower winds in the equatorial plane. Beyond  $10R_{\odot}$ , the winds are accelerated to approximately  $400 \text{ km s}^{-1}$  in the equatorial plane, and reach  $800 \text{ km s}^{-1}$  or higher in the outer corner regions of the domain. Polar winds are present at velocities of approximately  $600 \text{ km s}^{-1}$ . For this system, the ML rate is  $6.4 \times 10^{-14} M_{\odot} \text{ yr}^{-1}$  and the AML rate is  $4.9 \times 10^{30} \text{ g cm}^2 \text{ s}^{-2}$ . By comparison, the Sun’s ML rate is  $2 \times 10^{-14} M_{\odot} \text{ yr}^{-1}$  (Cohen et al. 2012), however, we expect our value to be higher since we are using a slightly larger magnetic field than the large scale solar field of approximately 5G.

#### 4.1.2 Sets A, B, and C

Figures 3 and 4 show the aligned and anti-aligned cases for the orbital separation of  $5.0R_{\odot}$  for all sets. Due to the scaling up of the WD radii, the smallest WD field strength of 10G is chosen as it is equivalent to an equatorial field strength of  $B \sim 10^5 \text{ G}$  at the true size of the WD. The presence of the WD causes an area of slightly higher wind velocities just in front of the WD and a large area of low wind velocities behind the WD. In many cases the wind velocities in the polar regions are increased by the WD addition. As the WD and the secondary star magnetic fields interact, the secondary magnetic field lines become distorted and bend around the

WD, becoming closed. The closing of magnetic field lines occurs at different radii in different cases. Generally, field lines extending up to  $1.0R_{\odot}$  in front of the WD remain closed. They can then become open behind the WD, depending on the radii. For example, for separations up to  $5.0R_{\odot}$ , the field lines behind the WD are mostly closed. However, it is unlikely for them to be closed behind the WD at  $5.0 - 6.0R_{\odot}$ . This is because how far closed lines naturally reach in the single secondary star case constrains how far they will reach in cases involving a second body.

It is easier for anti-aligned cases to close field lines behind the WD. This is intuitive, as two anti-aligned dipoles will cancel more field lines naturally, leading to less open field lines. Over both alignments, Set B and C cases show larger areas of slow winds behind the WD than Set A cases. This can be explained by the fact that they have larger magnetic field strengths and higher masses involved which leads to more closing of field lines and therefore slower winds behind the WD. For Set B, the anti-aligned cases produced a smaller Alfvén surface and a smaller slow wind tail than the aligned cases.

Over all cases, we can see that whereas there is a large difference in wind solution between the Set C cases, there is *not* for the Set A cases which correspond to the lower magnetic field strength of 10G. The magnetic field is not as important in this regime and that the results for this set are likely to be more hydrodynamical. The Set C cases create a larger fluctuation in the solution due to the larger magnitude magnetic fields interfering more with the stellar wind. We notice some asymmetries in the wind solution — these are not due to the magnetic field alignment or the WD orbital separation. This is caused by the fact that two nearby magnetic dipoles cannot always create completely stable and symmetric solutions. When the slow wind connecting the WD and the secondary is symmetrical, the Alfvén surface looks more symmetrical and closer to the single secondary star case. However, when the same slow wind points in a certain  $z$ -direction, a more distorted Alfvén surface is formed.

A noteworthy effect for the Set C cases is that a wind velocity pattern very close to the WD emerges whereas it is not present at the lower magnetic field strengths of the Set A and B cases. This can be observed in the evolution of the time-dependent simulations. Areas of higher wind velocity appear and disappear in lobe-like structures. This is due to magnetic field lines crossing in and out of the  $y = 0$  plane as the wind flows around the WD, creating the illusion of a changing wind velocity. In fact, it is the direction of the wind velocity vectors which are changing.

Figures 5 and 6 for mass density reinforce what we have learned from the stellar wind solution. Inclusion of the WD creates an area of slow winds behind the WD which show up on the density figures in red. We observe that a larger magnetic field strength in Set C causes a larger interaction of dipolar fields, resulting in slower winds and more mass trapped behind the WD. As the stellar wind is made up of ionised particles with mass, the density solutions trace the areas of slowest wind velocity as they will coincide with areas of highest particle number density. Over all cases, anti-aligned alignments show the greatest areas of high density behind the WD, reflecting the fact that they more easily close magnetic field lines.

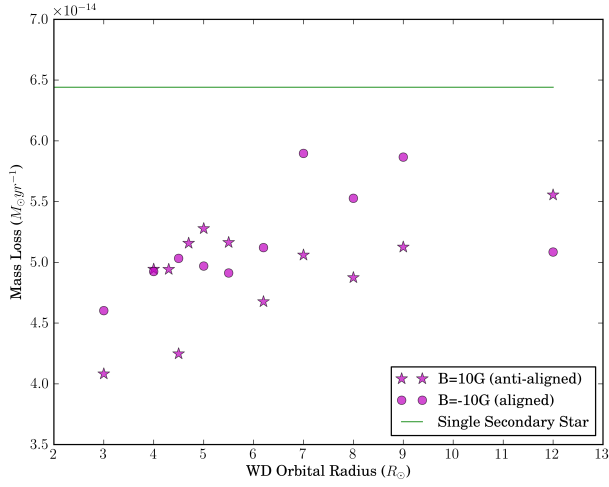


**Figure 8.** ML against orbital separation for the **Set A** cases, with the result for a single secondary star overlaid. Whilst both the aligned and anti-aligned cases show scatter, the aligned cases show the least. **I observe a trend of ML increasing with radii.**

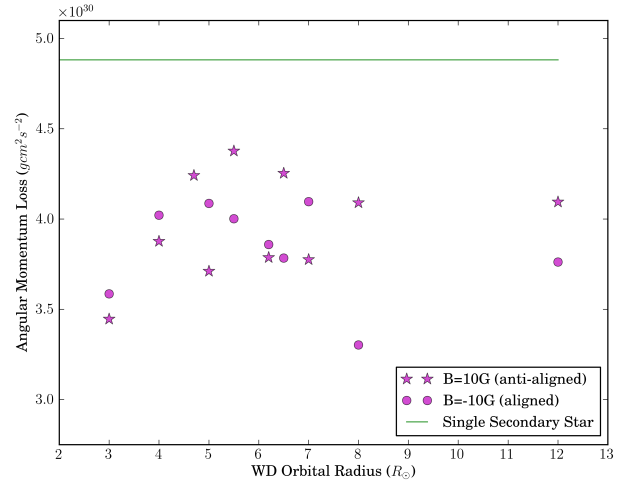


**Figure 11.** AML against orbital separation for the same **Set A** cases, with the result for a single secondary star overlaid. Similar to ML, **I observe a trend of AML increasing with radii.**

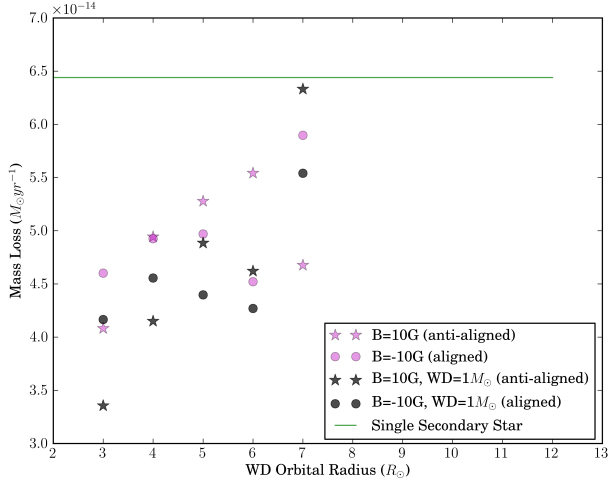


**Figure 9.** ML for the **Set B** cases in black. Over-plotted are the **Set A** cases. Again, we see a positive correlation between ML and orbital radius, with all cases possessing lower ML than the single secondary star case.

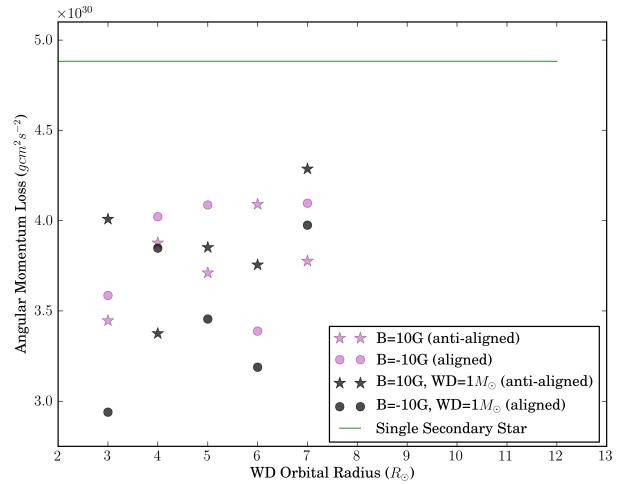


**Figure 12.** AML for the **Set B** cases in black. Over-plotted are the **Set A** cases for comparison.

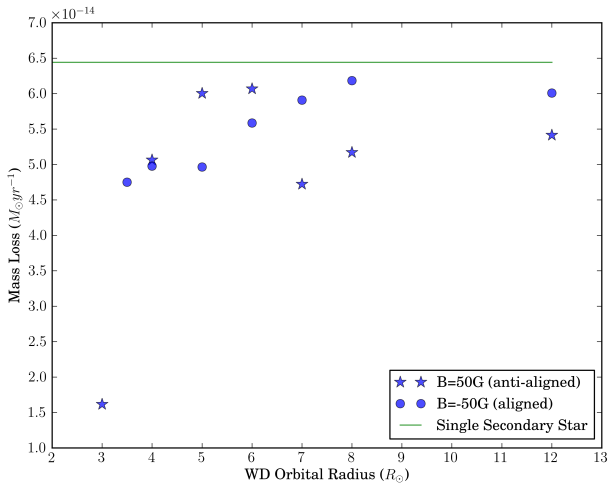


**Figure 10.** ML for the **Set C** cases. As with the other sets, there is a positive correlation present between ML and orbital radius.

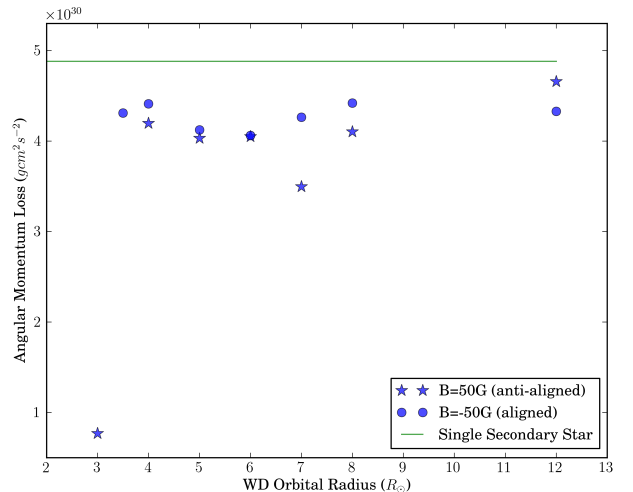


**Figure 13.** AML for the same **Set C** cases.

### 4.1.3 Time-Dependent Simulation

In Figure 7, I illustrate the time-dependent case at 2.5 hour intervals. As with all  $B = 50G$  solutions, we see a high velocity wind in front of the WD and a tail of slow winds behind, although in this case, the tail is more extended. The wind pattern indicates that there is magnetic reconnection and plasmoids present. The local wind solution near the WD varies whilst the overall solution remains relatively steady, suggesting that our ML rates are representative even though the variations in the solution with time show that it is a dynamic problem. However, the way that the Alfvén surface differs between solution explains the spread of the data for the AML rates, as they are calculated by integration over the Alfvén surface. The flow behind the WD looks similar to a turbulent wake behind a body, and we suggest that this is the 3-D manifestation of an instability such as the Kármán vortex street discussed in Section 1. The stellar wind is seen to move in an unsteady fashion as vortexes enter and leave the plane of view.

When calculating the average ML rate over this period of 13.2 hours, I find that the value remains close to the time-independent simulation value of  $6.0 \times 10^{-14} M_{\odot} \text{yr}^{-1}$  with a spread of  $0.29 \times 10^{-14} M_{\odot} \text{yr}^{-1}$ . This reconfirms our claim that even though there are fluctuations in the wind solution due to this being a dynamic problem, the overall ML rate remains relatively unchanged. The AML rate has a spread of  $1.4 \times 10^{30} \text{gcm}^2 \text{s}^{-2}$  around the previously calculated value of  $4.0 \times 10^{30} \text{gcm}^2 \text{s}^{-2}$ . The AML spread for time-dependent simulations is higher than the ML spread as the Alfvén surface is closer to the WD than where the ML rate is calculated at  $R = 58.0 R_{\odot}$ , and this area has the most variation in wind structure. The WD wind accretion values show more of a spread ( $2.8 \times 10^{-14} M_{\odot} \text{yr}^{-1}$ ) around the time-independent value of  $1.5 \times 10^{-14} M_{\odot} \text{yr}^{-1}$ . This represents the fact that the wind flow in close proximity to the WD evolves noticeably with time and the accretion rate varies accordingly.

## 4.2 Mass and Angular Momentum Loss Rates

As shown in Figures 3 and 4, the inclusion of the WD creates a decrease in stellar wind velocities in the region behind where the WD is placed and in some cases, an increase in stellar wind velocities in front of it. We propose that this is due to the WD magnetic field intervening, affecting the magnetic field structure, physically blocking the stream, and capturing charged material from the secondary. This, therefore, decreases the wind velocity behind the WD and accelerates some wind material towards the WD. As a consequence, **I find a reduction in ML rates over all test cases** when compared to the single secondary star reference case. This can be seen in Figures 8, 9, and 10. The green horizontal line represents the ML value for a single secondary, and I observe that all ML results from our simulations place below this line. We understand this to be linked to the slow winds — less charged material is reaching the higher velocities and therefore less escapes the entire system resulting in a reduction in ML rates. How quickly the system loses angular momentum is a consequence of wind-driven ML. I find that the presence of the WD can cause a decrease in AML of up to a factor of six compared with the single secondary star case. The WD magnetic field can also affect the Alfvén

surface and therefore the spin-down torque of the wind on the system.

I note that the greatest reduction in ML generally occurs for smaller orbital separations, regardless of magnetic field alignment. This is observed in Figures 8, 9, and 10 through a positive correlation between ML rate and orbital radius. This can be explained due to the fact that the further the WD is from the secondary, the less influence on the secondary’s stellar wind the WD magnetic field will have, and thus more material will pass by the WD undisturbed leading to a higher ML rate at larger separations. Smaller orbital separations cause more material to be attracted to the WD and therefore less is lost at the boundary of the domain. Additionally, I observe smaller ML rate values for the Set B cases when compared to the Set A cases. This result can quite easily be explained by the fact that the larger WD mass in the Set B cases cause a higher accretion rate and therefore a lower ML rate. Both of these observations can be confirmed by the WD wind accretion rates discussed in Section 4.3.

Magnetic field alignment also plays a role. For Set A cases at radii of 3.0, 4.5, 6.2, 7.0, 8.0, and  $9.0 R_{\odot}$ , the anti-aligned cases show larger ML reduction than the aligned cases when compared to the single secondary star case. For the remaining four cases, the opposite is true. However, for the Set B cases, anything larger than  $4.0 R_{\odot}$  shows a higher ML reduction for the aligned magnetic fields. This change of behavior is spatially coincidental with the transition between closed and open field line regimes for this set. Set C cases generally mimic Set A, with a switch in which alignment produces the highest ML reduction for  $5.0 - 6.0 R_{\odot}$ . This also occurs in Set B except here it continues up to  $7.0 R_{\odot}$ . This may be an outlier, as we do not yet have data for Set B beyond this separation, in which case the trend is that aligned magnetic fields produce a higher ML reduction only over the range  $5.0 - 6.0 R_{\odot}$ . The case of  $4.0 R_{\odot}$  has very similar values for ML for both alignments across both Set A and C, suggesting that the turnover is in fact near  $4.0 R_{\odot}$ .

**I find that inclusion of the WD can reduce the ML rate by up to  $4.8 \times 10^{-14} M_{\odot} \text{yr}^{-1}$**  (for Set C) when compared to the single secondary star case — a factor of four. For Set A, the biggest reduction is  $2.4 \times 10^{-14} M_{\odot} \text{yr}^{-1}$ , whilst for Set B it is  $3.1 \times 10^{-14} M_{\odot} \text{yr}^{-1}$ . These are all less than the order of magnitude previously found by Cohen et al. (2012). However, the models they were using are not as physically accurate as the BATS-R-US model that we use here.

For the AML rates, I observe a similar trend to that of ML but with more scatter. Over all cases, I observe a reduction in AML rate and in general, increasing the WD separation increases the AML rate. The scatter is due to the fact that the area over which the AML rate is calculated varies substantially more than the area over which the ML rate is calculated. Previously mentioned hydrodynamic fluctuations can cause the Alfvén surface to momentarily change (see Figure 7), yielding a different AML rate.

Increasing the WD mass brings about a decrease in AML rate as it did for ML rate. In Sets A and C, I observe that anti-aligned magnetic fields bring about a larger decrease in AML rate, whilst for Set B it is the opposite. For ML, this was only true for the larger separation end of the Set B cases. **I find that inclusion of the WD can**

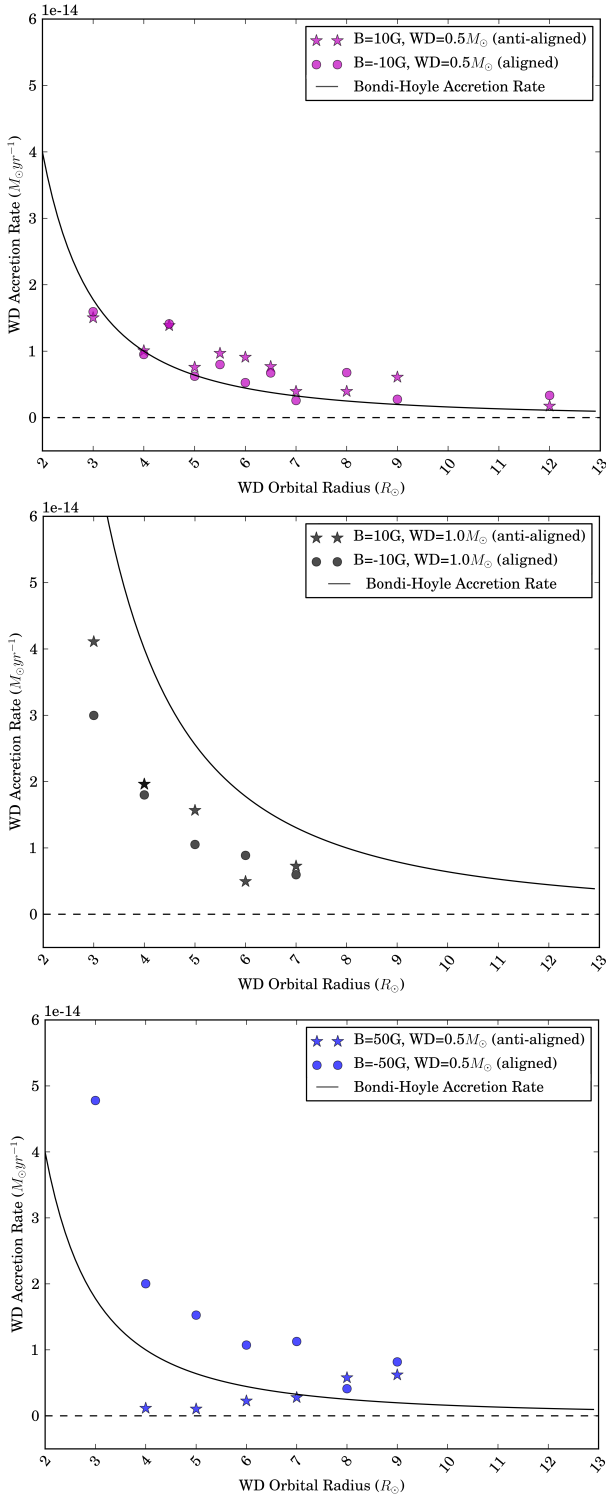


**Figure 14.** I display the WD wind accretion (in  $M_{\odot} \text{yr}^{-1}$ ) over a range of orbital separations. This is shown for the Set A, B, and C cases in the top, middle, and bottom panels respectively. Overlaid is the Bondi-Hoyle accretion rate calculated at each radii (Equation 8).

reduce the angular momentum loss rate by up to  $4.1 \times 10^{30} \text{gcm}^2 \text{s}^{-2}$  (for Set C) when compared to the single secondary star case — a factor of six. For Set A, the biggest reduction is  $1.5 \times 10^{30} \text{gcm}^2 \text{s}^{-2}$ , whilst for Set B it is  $1.9 \times 10^{30} \text{gcm}^2 \text{s}^{-2}$ . Again, these are all less than the order of magnitude previously found by Cohen et al. (2012). In both ML and AML, we can conclude that increasing the WD magnetic field strength or mass results in a larger reduction in mass or angular momentum. We argue that this reduction should be considered in future calculations for CV orbital evolution which include an AML prescription.

### 4.3 Wind Accretion of the White Dwarf

I explore the effect of different masses, magnetic configurations, and orbital separation on mass accretion of the secondary star onto the WD. I plot the WD accretion rate against WD orbital radius for all sets in Figure 14. To aid in the visualisation of our solutions, I plot the 3-D solution for the anti-aligned Set A case at an orbital separation of  $3.0R_{\odot}$  in Figure 15. The background is coloured by density and shows how the presence of the WD distorts the matter around the secondary such that it lowers the density near the WD poles and creates slightly higher density behind the WD. The largest rate of accretion is seen on the sides directly facing and facing away from the secondary star. The WD itself is coloured by mass flow, and shows the wind accretion, with dark green representing inflow, purple representing outflow, and white representing net zero flow.

As a visual representation of the wind accretion, I colour the  $0.75R_{\odot}$  shell by mass flow, with orange representing inflow, purple representing outflow, and white representing net zero flow. This is displayed in Figure 16 at a separation of  $3.0R_{\odot}$  for  $B = 10\text{G}$  and  $B = 50\text{G}$ . It is clear that the larger WD magnetic field produces a more complex pattern of wind accretion, as more field lines interfere with the stellar wind. Conversely, the  $B = 10\text{G}$  case, with its more homogeneous pattern, suggests that it is dominated by more of a hydrodynamical effect and that the field lines are not playing such an important role in funneling the accretion. As the WD orbital separation increases, I observe the same type of pattern evolving but with smaller overall mass inflow.

All cases in Figure 14 show a decreasing trend for WD wind accretion with increasing WD orbital separation, except for the anti-aligned case for Set C. A decreasing trend is to be expected logically because the closer the WD is to the secondary, the more stellar wind it will intercept and thus the higher the accretion rate. I observe the highest accretion rate of  $5.75 \times 10^{-14} M_{\odot} \text{yr}^{-1}$  for the aligned Set C case at  $3.0R_{\odot}$ . This may be the magnetic field effect kicking in while Sets A and B may be caused by hydrodynamical effects, as previously mentioned. For Set C, the separation between aligned and anti-aligned accretion decreases as the WD orbital radii increase, supporting the hypothesis that the change in trend between alignments here is caused by a magnetic interaction.

Additionally, accretion rates become larger with increasing WD mass, as you can see by comparing the magnitudes of the Set A and Set B cases. Theoretically, this should also be the case because a larger mass creates a larger gravitational potential and thus more matter is attracted. Increasing the field strength also increases the WD wind

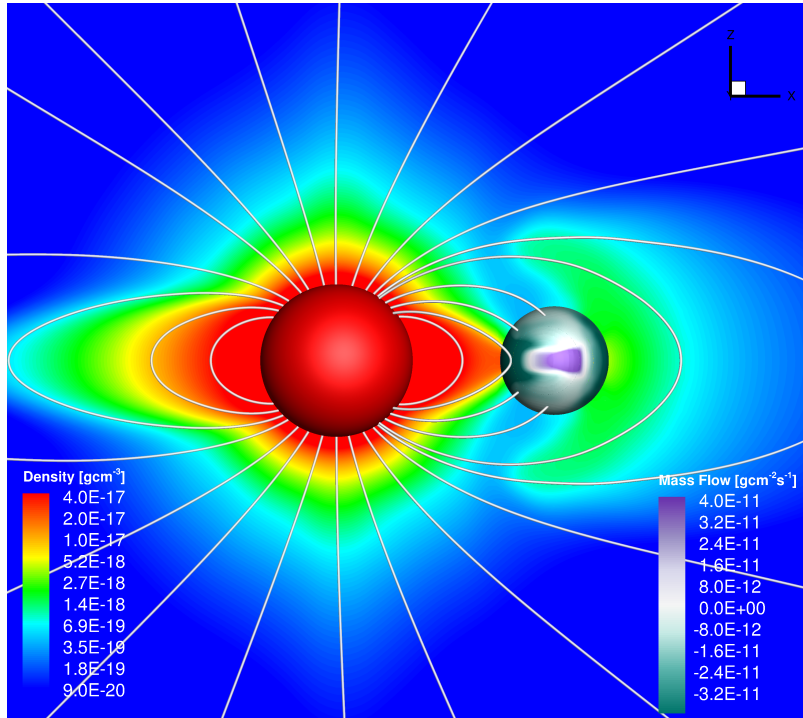


**Figure 15.** A 3-D view of the simulation with parameters of  $3.0R_{\odot}$  orbital separation, and  $B = 10\text{G}$ . The background is coloured by density and shows how the presence of the WD distorts the flow, or wind around the secondary. The WD is coloured by mass flow, and shows the wind accretion, with dark green representing negative velocity (inflow) and purple representing positive velocity (outflow).

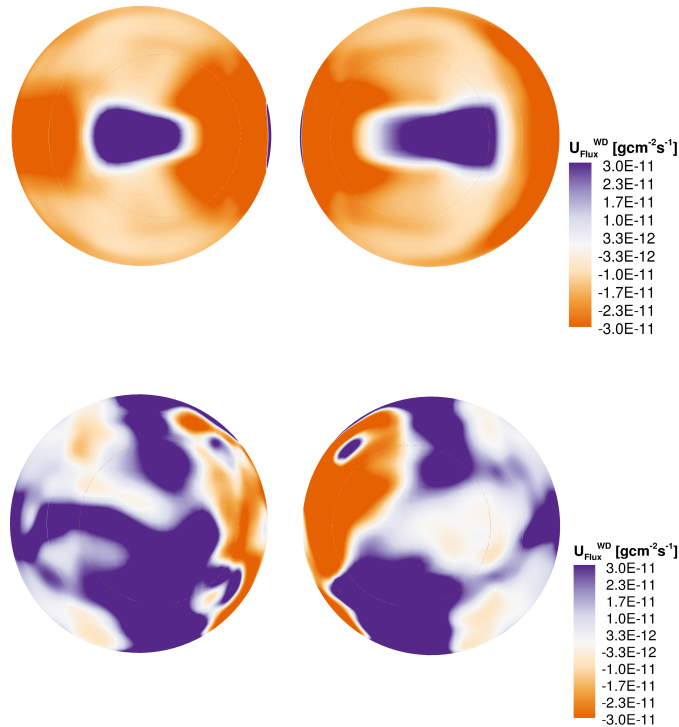


**Figure 16.** A sphere located at  $0.75R_{\odot}$  is drawn around the WD and coloured by mass flow,  $U_{\text{Flux}}^{\text{WD}}$ . This is shown from two orientations, separated by a rotation of  $\pi$  radians about the z-axis, such that the centre of both pairs of spheres represents the direction towards the secondary star. The top panel represents the case of  $B = 10\text{G}$  at  $3.0R_{\odot}$ , whilst the bottom panel represents the case of  $B = 50\text{G}$  also at  $3.0R_{\odot}$ . Purple represents outflow, whilst orange represents inflow.

accretion rate. This can be explained by the fact that the ionized gas is entrained by field lines. Therefore, a stronger field would have a longer reach, channeling wind over a larger volume and resulting in a greater accretion rate.

Field alignment also plays a role; I find that for the vast majority of cases, accretion is most efficient for anti-aligned magnetic field configurations. This makes sense physically — when the fields of the two stars are anti-aligned, field lines are closed more easily instead of being deflected, resulting in more efficient siphoning of charged material onto the WD. For all cases, I observe accretion rates of the order of  $10^{-14} M_{\odot} \text{yr}^{-1}$ .

## 5 SUMMARY

Through the use of 3-D magnetohydrodynamic simulations, we perform an investigation into a binary system consisting of a WD and a secondary star. Specifically, we aim to discover how the wind solution and mass loss rates are affected by variation of the WD mass, magnetic field strength and alignment, and orbital separation. The motivation is to advance our understanding of CV evolution in the parameter space above the period gap, where the main source of angular momentum loss is through the magnetised stellar wind, known as magnetic braking. Our approach is to examine the wind solutions of a set of time-independent and time-dependent simulations. Through integration over various surfaces, I extract the mass loss and WD wind accretion rates for each system and plot them against WD orbital separation to identify the trends present.

WD wind accretion rates decrease as orbital separation increases, and for all cases I find accretion rates of the order of  $10^{-14} M_{\odot} \text{yr}^{-1}$ . Field alignment plays a role here too — I find that accretion is most efficient for anti-aligned magnetic field configurations. This is due to the anti-aligned cases closing more magnetic field lines, resulting in more efficient siphoning of magnetic material onto the WD.

Inclusion of the WD can reduce the mass loss rate by up to a factor of four, when compared to a single secondary star case. The exact mass loss reduction depends on WD orbital separation, with the largest reduction occurring for the smallest separations. In the majority of cases, magnetic field strength and alignment also plays a role — I observe a larger reduction in mass loss for larger WD magnetic fields and over most separations, anti-aligned dipolar configurations result in a further reduction.

Inclusion of the WD can reduce the angular momentum loss rate by up to a factor of six, when compared to the single secondary star case. As with ML, these are all less than the order of magnitude previously found by Cohen et al. (2012) and we suggest this is because of model discrepancies between our two approaches, with our model being the most physical and up-to-date with solar observations. In both ML and AML, we can conclude that increasing the WD magnetic field strength or mass and decreasing WD separation results in a larger reduction in mass and angular momentum loss rates. We argue that this reduction should be considered in future calculations for CV orbital evolution which include an AML prescription. It is our hope that this work will serve as the foundations for many further simulation studies into CV orbital evolution.

## 5.1 Future Work

There are many ways in which to take this project further; the following are just a few that I believe would be the most interesting. For this study, I use a theoretical perfect dipole for the magnetogram. To add to the realism of the simulations, real magnetograms taken from Zeeman-Doppler Imaging (ZDI) could be used as the starting point for the secondary magnetic field. It would be interesting to investigate higher multipoles in order to examine what effect magnetic complexity has on ML and wind environment. We have only simulated perfect alignment or anti-alignment, and so a study considering alignments that are out of phase by angles different than  $\pi$  radians could be done. As previously mentioned, this occurs naturally as stellar cycles progress and so would be a useful addition. In this project, only magnetic field strengths of 10G and 50G were used. Future works could use higher magnetic field strengths and alternate magnetic field strength ratios for the WD and secondary.

Although a small selection of time-dependent runs were performed in this study, there was insufficient time to complete many cases. Future works could perform more time-dependent simulations — allowing them to run for a longer time period, and beginning them from different points during the time-independent simulation in order to see what effect this induces.

Another addition could be to include the rotation of the WD. This would cause different hydrodynamical effects as the stellar wind now passes over a spinning mass instead of a stationary one. The variations in wind structure behind the WD we observe in this investigation may be caused by the fact that the WD is assumed stationary as it orbits. If a spin was included in the simulation, then perhaps these wind structures behind the WD would be altered and we may achieve a higher level of realism. Further to this, the effect of changing the rotation period could be investigated.

This project looks only at a CV-like system, however, to simulate a solar system instead, more bodies could be added to represent planets. These simulations would give insight into the current problems in exoplanetary research, such as how the stellar wind environment changes over the lifetime of a star, and in which cases might it be preferable for an atmosphere habitable for life to form.

Any one of these additions would require many time-dependent and time-independent simulations and the subsequent analysis. We have illustrated that by using BATS-R-US, a steady solution can be found and the wind environment as well as the ML and AML rates can be extracted. Therefore, I believe that this project forms a good basis in which to work from. It would be relatively simple to extend this work to some of the cases listed above in an attempt to answer some of the intriguing questions still remaining in this field.

**ACKNOWLEDGMENTS**

I extend my sincere gratitude to Cecilia Garraffo for supervising me throughout this project. Her help in teaching me how to plan and execute the simulations and her guidance on the types of things to look out for was invaluable. In addition, I would like to thank Jeremy Drake and Diego Alvarado-Gomez for their help on a multitude of issues and for making this work a reality through their efficient coordination of my Master's course. Thank you to Ofer Cohen and Julian Alvarado-Gomez for their input on how to get the simulations to run correctly and displaying solutions. Finally, thank you to my course mates — Chris Desira, Florence Concepcion Mairey, Claire Baker, and Anna Laws for their support throughout this year. There are many others who have helped me along the way, but at the risk of this turning into an Oscar acceptance speech, I will conclude here.

**REFERENCES**

- Andronov, N., Pinsonneault, M., & Sills, A. 2003, *ApJ*, 582, 358
- Arge, C. N. & Pizzo, V. J. 2000, *J. Geophys. Res.*, 105, 10465
- Barnes, S. A. 2003, *ApJL*, 586, L145
- Bondi, H. & Hoyle, F. 1944, *MNRAS*, 104, 273
- Cohen, O., Drake, J. J., & Kashyap, V. L. 2012, *ApJL*, 746, L3
- Davis, P. J., Kolb, U., Willems, B., & Gänsicke, B. T. 2008, *MNRAS*, 389, 1563
- Debes, J. H. 2006, *ApJ*, 652, 636
- Drake, J. J., Garraffo, C., Takei, D., & Gaensicke, B. 2014, *MNRAS*, 437, 3842
- Ivanova, N. & Taam, R. E. 2003, *ApJ*, 599, 516
- Kawaler, S. D. 1988, *ApJ*, 333, 236
- Knigge, C. 2006, *MNRAS*, 373, 484
- Knigge, C. 2011, in *Astronomical Society of the Pacific Conference Series*, Vol. 447, *Evolution of Compact Binaries*, ed. L. Schmidtbreick, M. R. Schreiber, & C. Tappert, 3
- Kraft, R. P., Mathews, J., & Greenstein, J. L. 1962, *ApJ*, 136, 312
- Matranga, M., Drake, J. J., Kashyap, V., & Steeghs, D. 2012, *ApJ*, 747, 132
- Mestel, L. 1968, *MNRAS*, 138, 359
- Mestel, L. 1999, *Stellar Magnetism*
- Powell, K. G., Roe, P. L., Linde, T. J., Gombosi, T. I., & Zeeuw, D. L. D. 1999, *Journal of Computational Physics*, 154, 284
- Rappaport, S., Verbunt, F., & Joss, P. C. 1983, *ApJ*, 275, 713
- Riess, A. G., Filippenko, A. V., Challis, P., et al. 1998, *AJ*, 116, 1009
- Schatzman, E. 1962, *Annales d'Astrophysique*, 25, 18
- Than, K. 2013, *Sun's Magnetic Field to Reverse: What It Means*, <http://news.nationalgeographic.com/news/2013/08/130807-sun-magnetic-field-reversal-space-weather/>, (accessed May 5, 2017)
- Tóth, G., van der Holst, B., Sokolov, I. V., et al. 2012, *Journal of Computational Physics*, 231, 870, special Issue: *Computational Plasma Physics*
- van der Holst, B., Sokolov, I. V., Meng, X., et al. 2014, *ApJ*, 782, 81
- Verbunt, F. & Zwaan, C. 1981, *A&A*, 100, L7
- Wang, Y.-M. & Sheeley, Jr., N. R. 1990, *ApJ*, 355, 726
- Wargelin, B. J., Saar, S. H., Pojmański, G., Drake, J. J., & Kashyap, V. L. 2017, *MNRAS*, 464, 3281
- Weber, E. J. & Davis, Jr., L. 1967, *ApJ*, 148, 217
- Wood, B. E., Linsky, J. L., Müller, H.-R., & Zank, G. P. 2001, *ApJL*, 547, L49
- Wright, N. J., Drake, J. J., Drew, J. E., & Vink, J. S. 2012, *Astrophysics and Space Science Proceedings*, 29, 179